The Role of Collinear Interaction in Dislocation-Induced Hardening

R. Madec,[1]* B. Devincre,[1] L. Kubin,[1]† T. Hoc,[2] D. Rodney[3]

We connected dislocation-based atomic-scale and continuum models of plasticity in crystalline solids through numerical simulations of dislocation intersections in face-centered cubic crystals. The results contradict the traditional assumption that strain hardening is governed by the formation of sessile junctions between dislocations. The interaction between two dislocations with collinear Burgers vectors gliding in intersecting slip planes was found to be by far the strongest of all reactions. Its properties were investigated and discussed using a multiscale approach.

Plastic flow in crystalline materials is intimately related to the generation, motion, and storage of linear defects, known as dislocations. These defects connect two areas of the crystal that are sheared with respect to each other by an atomic translation called the Burgers vector. They locally disrupt the ordering of the atoms in a crystal and induce long-range stress and strain fields. Under an externally applied stress, dislocations interact and multiply in crystallographic slip planes, producing plastic deformation through the accumulation of atomic shears. In all crystalline materials, including alloys and compounds, strain hardening occurs because of the increased number of interacting dislocations that trap each other in minimum energy configurations (*1*). In face-centered cubic (fcc) crystals, these interactions occur between 12 slip systems that involve {111} slip planes and 1/2⟨110⟩ Burgers vectors. The prevailing view has been that reactions between intersecting dislocations leading to the formation of stable barriers, notably the Lomer-Cottrell lock, govern the flow stress in multislip conditions (*2*). The present investigation, which combines simulations at different scales, shows that this belief is partly incorrect, in that the strongest reaction has thus far been neglected.

Theoretical and experimental investigations agree that the flow stress of pure fcc crystals is inversely proportional to the average distance between obstacles in the slip planes and is therefore proportional to the square root of the dislocation density (*2*–*5*). However, in this global relation, the strengths of all interactions are lumped into a single proportionality coefficient. To predict the number and nature of active slip systems, a more sophisticated relation must be employed, where the dislocation density is decomposed into densities per slip system. With ρ^s denoting the density on slip system (s) and τ_c^s the critical resolved shear stress for dislocation motion in this system, we have (*6*)

$$\tau_c^s/\mu = b\sqrt{\sum_u a^{su}\rho^u} \qquad (1)$$

where the summation is carried out over all slip systems (u). b is the modulus of the Burgers vector, and μ is the shear modulus. For elastically anisotropic crystals, the effect of anisotropy is averaged out in large dislocation densities and μ is an isotropic average shear modulus. $[a^{su}]$ is a dimensionless interaction matrix expressing the average strength of the interactions and reactions between slip systems.

By reason of symmetry, the interaction matrix $[a^{su}]$ has only six independent coefficients. Two of them involve only elastic interactions between dislocations gliding in parallel slip planes. Because these interactions are weak (*3*, *4*), their properties are not reported here. Three intersections form stable junctions; namely, the Hirth lock, the glissile junction, and the Lomer-Cottrell lock, which is thought to be the strongest. The corresponding configuration formed with perfect nondissociated dislocations is called the Lomer lock. Lomer and Lomer-Cotrell locks have been the subject of several recent investigations (*5*, *7*–*9*) by atomistic and dislocation dynamics simulations (DDSs) at the mesoscale, which showed that they have practically the same strength. The reason is that the contribution of the dislocation core to the self energy of a dislocation line is small enough to be neglected (*1*). Owing to the very large self energy of a dislocation, typically μb^3 per atomic length of line, thermal fluctuations do not contribute significantly to junction destruction. This justifies estimating "forest" hardening within an elastic athermal framework and with perfect dislocations, as in earlier calculations (*1*, *2*).

The sixth interaction coefficient corresponds to the so-called collinear interaction between dislocations of parallel Burgers vectors gliding in intersecting slip planes, each plane being the cross-slip plane of the other. This interaction has not been studied in detail and is assumed to be of weak or intermediate strength (*3*, *4*, *6*, *10*). Two experimental observations are available. One is concerned with strained SiGe/Si epitaxial layers (*11*), where dislocations of same Burgers vectors tend to accumulate at the film/substrate interface, thus increasing the visibility of the collinear interaction. The other (*12*) was obtained by deforming an Al-Mg alloy in situ in a transmission electron microscope (fig. S1).

The average strength of the various dislocation interactions is difficult to estimate from theory or extract from experiments (*3*, *6*, *10*), but can be evaluated by DDS. We employ a three-dimensional DDS (*13*), in which connected segments describing perfect dislocation lines are embedded into an elastic continuum. These segments move by discrete crystallographic steps, and the level of discretization is adjusted to the scale of the investigated configuration (*5*). The interaction coefficients of Eq. 1 were evaluated from model simulations in which the interacting dislocations were chosen so that only one type of reaction occurred at a time. The simulated fcc crystal contained a few long mobile dislocation lines on one system and a random distribution of forest segments on other slip systems, producing a specific type of reaction with the mobile dislocations. A constant strain rate was applied, which induced a resolved shear stress on the mobile dislocations, whereas the forest systems were not activated. The model material had the isotropic elastic constants and Burgers vector of copper. The interaction coefficients were deduced from Eq. 1 by the simultaneous measurement of the resolved applied stress and the forest density.

Figure 1A shows the traditional picture of a dislocation moving through a forest, by the formation and destruction of junctions. By way of contrast, in the case of the collinear interaction shown in Fig. 1B, the

[1]Laboratoire d'Etude des Microstructures, UMR 104 CNRS, CNRS-ONERA, 20 Avenue de la Division Leclerc, BP 72, 92322 Chatillon Cedex, France. [2]Laboratoire Mécanique des Sols, Structures et Matériaux, UMR 8579 CNRS, Ecole Centrale Paris, Grande Voie des Vignes, 92295 Chatenay-Malabry Cedex, France. [3]Génie Physique et Mécanique des Matériaux, UMR 5010 CNRS, ENSPG, Domaine Universitaire, 38402 St. Martin d'Hères Cedex, France.

*Present address: Département de Physique Théorique et Appliquée, Commissariat à l'Energie Atomique, BP 12, 91680 Bruyères-le-Châtel, France.
†To whom correspondence should be addressed. E-mail: kubin@onera.fr

moving line undergoes successive partial annihilations with the attractive "trees," resulting in the formation of many small residual segments (Fig. 2, A and E). To accommodate the imposed strain rate, these segments have to be remobilized, which requires an activation stress that is inversely proportional to their length. Thus, in qualitative terms, the exhaustion of the mobile density and the need to generate mobile segments result in a much higher applied stress, as compared to all other junction-forming interactions. Values of the dimensionless coefficients of the interaction matrix for the four reactions mentioned above are given in Table 1. They are rather insensitive to the degree of organization of the dislocation microstructure, as shown in (*5*). These values slightly depend on the density of forest obstacles, as discussed below (Eq. 2), and are given here for a density of 10^{12} m^{-2}.

The values of the measured interaction coefficients corresponding to the three junctions agree with the hierarchy of strengths deduced from latent hardening experiments (*3*, *6*, *10*). Moreover, in agreement with the qualitative arguments given above, the coefficient of the collinear interaction appears to surpass all the other coefficients.

To ascertain that dislocation dissociation does not result in atomic-scale configurations that affect the properties of the collinear annihilation, we investigated the evolution of two straight segments cutting each other at their midpoint, using both DDS and molecular static simulations (MSSs); that is, atomic-scale simulations where equilibrium configurations of minimum energy are obtained between increments of applied shear strain (*13*). Elastic anisotropy may influence the properties of individual configurations. For that reason and to help comparisons between MSS, which includes anisotropy, and DDS, which uses isotropic elasticity, the simulations were performed on aluminum, which is almost isotropic. In both simulations, a shear stress was applied along the same orientation. The common initial configuration consisted of two straight dislocation lines 27 nm in length, shown as dotted lines in Fig. 2E. In the MSS, a semi-empirical embedded atom method was employed as in earlier studies of junctions (*8*). The two simulations differed only in the boundary conditions (*13*). Rigid conditions were used in the MSS in order to pin the dislocation lines at their extremities and measure their remobilization stress. In the DDS, the segments were also pinned at their ends, and remote periodic conditions were used.

Partial annihilation of the lines produces composite dislocations made of two segments, one in each slip plane, connected by a

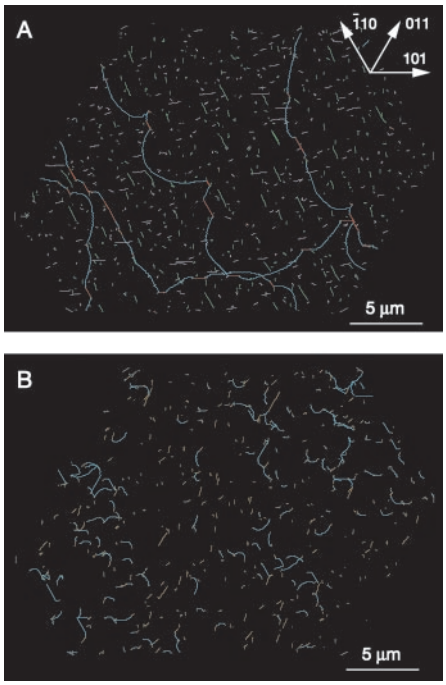

Fig. 1. Non-coplanar interactions between slip systems. Dislocations (blue lines) of Burgers vector 1/2[011] glide in (11$\bar{1}$) slip planes and interact with randomly distributed forest segments 2 μm in length. The figures show (11$\bar{1}$) thin films of thickness 0.1 μm extracted from the simulations. (**A**) Formation of Lomer locks (straight red segments) through the interaction with a forest of 1/2[110](1$\bar{1}$1) and 1/2[$\bar{1}$01](111) dislocations. (**B**) Collinear interaction with a forest of 1/2[011] dislocations gliding in the (1$\bar{1}$1) cross-slip plane of the mobile dislocation.

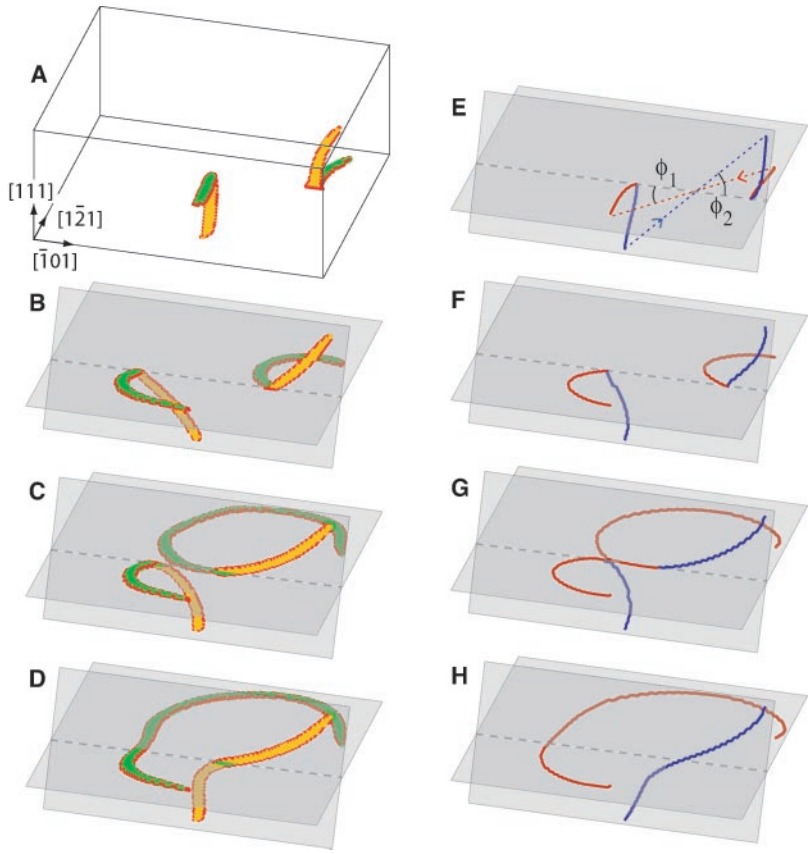

Fig. 2. Simulations of the collinear interaction in aluminum. Two segments [dotted lines in (E); the arrows show the positive sense on the lines] with collinear Burgers vectors 1/2[$\bar{1}$01](111) and 1/2[$\bar{1}$01](1$\bar{1}$1) make angles of $\phi_1 = \phi_2 = \pi/4$ with the [$\bar{1}$01] intersection of the two slip planes (dashed lines). An increasing strain (from top to bottom), is applied in the (111) plane, parallel to the common Burgers vector. Left column: MSS. The dislocation stacking faults are visualized by showing only the atoms with a non-fcc local environment. Right column: DDS. The two initial segments are shown with different colors. (**A** and **E**) Initial configuration after annihilation and without applied loading. (**B** and **F**) Critical configurations under stress. (**C**, **G**, **D**, and **H**) Recombination and remobilization of the two initial segments.

Table 1. Dimensionless coefficients of the interaction matrix for fcc crystals.

Type of interaction	Hirth lock	Glissile junction	Lomer lock	Collinear interaction
Value	0.051 ± 0.012	0.075 ± 0.014	0.084 ± 0.012	1.265 ± 0.125

node along the intersection line between the slip planes (Fig. 2, A and E). As mentioned, reaction decreases the mobile dislocation length, as seen when comparing the initial and final lengths of the dislocation segments. However, the collinear annihilation can also be viewed as forming a junction of zero Burgers vector and therefore zero elastic energy, implying that it is the most stable possible reaction. Figure 2 shows excellent agreement between the dislocation configurations obtained from MSS and DDS. Moreover, for the configurations of Fig. 2, B and F, which correspond to the critical remobilization stress, the reduced stress values are $\tau_c/\mu = 1.85 \times 10^{-2}$ for the MSS and $\tau_c/\mu = 1.67 \times 10^{-2}$ for the DDS. The small difference is attributed to the use of different boundary conditions in the two simulations. These agreements confirm the absence of any atomic-scale configuration to be accounted for at an upper scale.

The critical remobilization stress of a dislocation segment of length l is written in the dimensionless form (*1*, *4*, *14*)

$$\tau_c = K\frac{\mu b}{l} ln(\frac{l}{b}) \qquad (2)$$

where the logarithmic term includes inner and outer cut-off radii for the elastic field and K is a constant. Because the length l of the segments produced by a collinear annihilation is geometrically related to the initial length l_0 of the interacting segments, this expression allows one to rescale the critical stresses for any value of l_0 or of the forest density, $\rho \propto l_0^{-2}$. Thus, the coefficients of the interaction matrix given in Table 1 depend in a logarithmic manner on the forest density.

To complete this study, the dependence of the collinear annihilation on the orientation of the dislocation lines was investigated and compared to similar investigations on the Lomer lock (*5*). We carried out DDS on pairs of interacting segments like those of Fig. 2, 1 μm in length, initially making variable angles ϕ_1 and ϕ_2 with respect to the direction of their common Burgers vector. The result is plotted in Fig. 3 in the form of a mapping, where the symbols represent the final result of the interaction. Although half of the initial configurations correspond to segments that elastically repel each other, collinear annihilations appear in a vast majority in the relaxed configurations. The reason is that the flexibility of the lines allows them, through bending and twisting, to reach the minimum energy configuration corresponding to mutual annihilation. One also finds repulsive configurations and crossed states (*15*), where dislocation segments weakly interact (*14*). A graph similar to that of Fig. 3, drawn for the Lomer lock (*5*), shows that junction formation is restricted to only about 25% of the configurations. Thus, the high strength of the collinear reaction is due not only to its intrinsic stability, but also to its very high probability of occurrence.

Several consequences can be deduced from the present study, which we believe apply to all crystalline structures, although only fcc crystals are discussed here. The collinear interaction is expected to strongly influence the mechanical properties of crystals stressed along high-symmetry orientations, where slip and cross-slip systems have same resolved shear stresses, such as [100] or [111]. Figure 4 shows the stress-strain curve obtained from the DDS for a copper crystal deformed along a [100] orientation (*13*). It was found that with increasing strain, four out of the eight initially active slip systems became inactive, which were the cross-slip systems of the four other systems. Dislocation densities and strains were recorded for all the slip systems. Inserting their values into Eq. 1 and making use of the interaction coefficients of Table 1, the strain dependencies of the critical activation stresses of the slip systems were reconstructed. From the reconstructed curves shown in Fig. 4, one can see that the stress-strain curves cannot be reproduced in the absence of the collinear interaction. In addition, in the presence of the collinear interaction, the simultaneous activation of both the slip and cross-slip systems is predicted to be unstable. Indeed, the critical resolved shear stress, as given by Eq. 1, favors the activation of those slip systems that experience the weakest global interaction with the microstructure. The same holds for grains of polycrystals, which can be thought of as a composition of single-crystal properties in multislip conditions (*16*). Thus, the collinear interaction affects plastic flow in multislip conditions by selecting one combination of slip systems among all possible ones.

The collinear interaction, which promotes local rearrangements, annihilations, and blocking effects, also affects the recovery and relaxation properties of dislocation microstructures, in static conditions or under stress. This was suggested in different contexts by Jackson (*17*) and Stach *et al.* (*18*), who discussed mechanisms involving collinear annihilation under the name of exchange interaction and reactive blocking, respectively.

Therefore, owing to its considerable contribution to multislip hardening and its influence on the selection of active slip systems, the collinear interaction appears to deserve much more attention than it has been given up to now and provides a reason to revisit the traditional picture of strain hardening entirely governed by junction properties (*1–4*, *14*). Moreover, the interaction matrix of Table 1, which is evaluated from parameter-free DDS, is valid for all fcc crystals and is a fundamental constituent of physically based predictive models of plastic deformation at the macroscale.

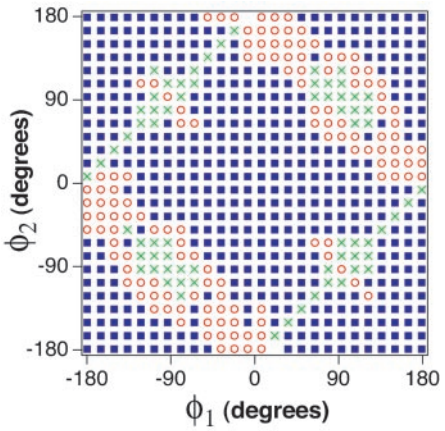

Fig. 3. Mapping of the collinear interaction in fcc crystals. The two interacting segments have opposite Burgers vector $b_1 = -b_2 = 1/2[011]$ and make variable angles, ϕ_1 in $(1\bar{1}\bar{1})$ and ϕ_2 in $(11\bar{1})$, with respect to the intersection of their slip planes (Fig. 2). The initially straight segments are pinned at their ends, and their length is $l_0 = 1$ μm. The model material is copper. The symbols indicate the nature of the final configuration: squares, collinear annihilation; circles, repulsive interaction; crosses, crossed state.

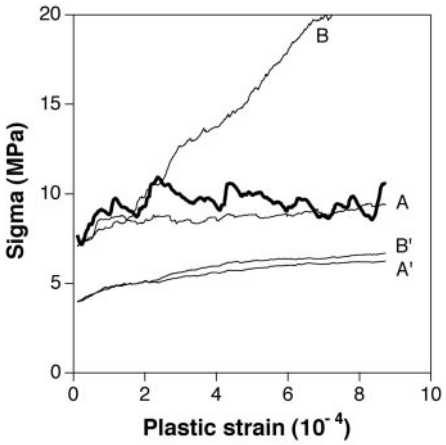

Fig. 4. Bold curve: [100] stress-strain curve obtained from the DDS for a copper crystal of size $(10\ \mu m)^3$, using periodic boundary conditions. Curve A shows the reconstructed strain dependency of the critical stress for one of the four active slip systems. This curve matches the result of the "mass" simulation, confirming that this system should be active. Curve B is for one of the cross-slip systems that becomes inactive. As expected, the critical stress increases above the applied stress. Curves A′ and B′ refer to the same slip systems as A and B but were obtained by omitting the collinear interaction. The predicted critical stresses are far below the applied stress.

References and Notes

1. J. Friedel, *Dislocations* (Pergamon, Oxford, 1967).
2. G. Saada, *Acta Metall.* **8**, 441 (1960).
3. S. J. Basinski, Z. S. Basinski, in *Dislocations in Solids*,

F. R. N. Nabarro, Ed. (North Holland, Amsterdam, 1979), vol. 4, pp. 261–362.
4. J. Gil Sevillano, in *Materials Science and Technology*, H. Mughrabi, Ed. (VCH, Weinheim, Germany, 1993), vol. 6, pp. 19–88.
5. R. Madec, B. Devincre, L. P. Kubin, *Phys. Rev. Lett.* **89**, 255508 (2002).
6. P. Franciosi, M. Berveiller, A. Zaoui, *Acta Metall.* **28**, 273 (1980).
7. V. V. Bulatov, F. F. Abraham, L. P. Kubin, B. Devincre, S. Yip, *Nature* **391**, 669 (1998).
8. D. Rodney, R. Phillips, *Phys. Rev. Lett.* **82**, 1704 (1999).
9. V. B. Shenoy, R. V. Kukta, R. Phillips, *Phys. Rev. Lett.* **84**, 1491 (2000).
10. J. L. Bassani, T. Y. Wu, *Proc. R. Soc. London Ser. A* **435**, 21 (1991).
11. E. A. Stach *et al.*, *Philos. Mag. A* **80**, 2159 (2000).
12. M. J. Mills, unpublished data.
13. Methods are available as supporting material on *Science* Online.
14. G. Schoeck, R. Frydman, *Phys. Stat. Sol. B* **53**, 661 (1972)
15. L. K. Wickham, K. W. Schwarz, J. S. Stölken, *Phys. Rev. Lett.* **83**, 4574 (1999).
16. S. Hansen, X. Huang, *Acta Mater.* **46**, 1827 (1998).
17. P. J. Jackson, *Progr. Mat. Sci.* **29**, 139 (1985).
18. E. A. Stach, K. W. Schwarz, R. Hull, F. M. Ross, R. M. Tromp, *Phys. Rev. Lett.* **84**, 947 (2000).

Supporting Online Material
www.sciencemag.org/cgi/content/full/301/5641/1879/DC1
Methods
Fig. S1
References

9 April 2003; accepted 14 August 2003

DNA-Templated Self-Assembly of Protein Arrays and Highly Conductive Nanowires

Hao Yan,[1]* Sung Ha Park,[1,2] Gleb Finkelstein,[2] John H. Reif,[1] Thomas H. LaBean[1]*

A DNA nanostructure consisting of four four-arm junctions oriented with a square aspect ratio was designed and constructed. Programmable self-assembly of 4 × 4 tiles resulted in two distinct lattice morphologies: uniform-width nanoribbons and two-dimensional nanogrids, which both display periodic square cavities. Periodic protein arrays were achieved by templated self-assembly of streptavidin onto the DNA nanogrids containing biotinylated oligonucleotides. On the basis of a two-step metallization procedure, the 4 × 4 nanoribbons acted as an excellent scaffold for the production of highly conductive, uniform-width, silver nanowires.

DNA, well known as the predominant chemical for duplication and storage of genetic information in biology, has also been shown to be highly useful as an engineering material for construction of micrometer-scale objects with nanometer-scale feature resolution. Self-assembling nanostructures composed of DNA molecules offer great potential for bottom-up nanofabrication of materials and objects with ever smaller features. Potential applications of DNA self-assembly and scaffolding include nanoelectronics, biosensors, and programmable/autonomous molecular machines. Recently, DNA has been used in the construction of periodically patterned structures (*1–7*), nanomechanical devices (*8–12*), and molecular computing systems (*13–17*). DNA has also been employed, with appropriate attachment chemistries, to direct the assembly of other functional molecules (*18–27*). A variety of unusual DNA motifs (*28*) whose designs are based on the immobile DNA branched junction, a stable analog of the Holliday intermediate from genetic recombination, have been used for self-assembly of periodic or aperiodic arrays (*3–7*).

Here we describe the design and construction of a DNA nanostructure that has a square aspect ratio and readily self-assembles into two distinct lattice forms: nanoribbons or two-dimensional (2D) nanogrids. The 4 × 4 tile (Fig. 1A) contains four four-arm DNA branched junctions pointing in four directions (north, south, east, and west in the tile plane). It is composed of nine strands, with one of the strands participating in all four junctions. Bulged T_4 loops were placed at each of the four corners inside the tile core to decrease the probability of stacking interactions between adjacent four-arm junctions and to allow the arms to point to four different directions. Although individual branched junctions are expected to be fairly flexible, when constrained by three additional junctions within the tile and a further junction in a neighboring tile, the structure is sufficiently rigid to act as a building block in larger superstructures. Characterization of the annealed structure by nondenaturing gel electrophoresis and thermal transition analysis shows that the 4 × 4 tile is stable and well behaved (fig. S1).

Based on the structure shown in Fig. 1A, two other versions of the 4 × 4 tile with redesigned sticky ends were prepared, assembled, and visualized by atomic force microscopy (AFM) (*29*). By reprogramming the sticky-end associations to vary the assembly strategy, we were able to control the preferred lattice formation. Both designs resulted in lattices containing periodic square cavities. One strategy (the original design) produced a high preponderance of uniform-width ribbon structures (Fig. 1B). In this design, the distance between adjacent tile centers is an even number of helical half-turns (four full turns) so that the same face of each tile points toward the same lattice face. Figure 1B shows a schematic drawing of the tile and assembly as well as three AFM images of the nanostructures formed from the original design. Self-assembly based on the original design resulted in long (average ~5 μm) ribbon-like lattices with uniform width (~60 nm). The regularity of the periodic cavities is pronounced, as well as the observation that some of the nanoribbons revealed a single-layer flat grid lattice unrolled at the open end of the ribbon. This observation strongly suggests that the ribbon structure results from tube-like structures that flatten when the sample is deposited on mica. The AFM height profile clearly shows that the nanoribbon structure has two layers compared to the flat lattice (fig. S2). Also, the edges of the ribbon appear slightly higher (~0.12 nm) than the middle, indicating a finite radius of curvature for the squashed tube structure (fig. S2). One reason for the formation of tube-like lattices could be that each component tile is designed to be oriented in the same direction in the lattice plane; therefore, any incidental curvature resident in each tile would accumulate and cause circularization of the lattice (see proposed model in fig. S3). This hypothesis is tested and supported by the corrugated design described below.

The second design strategy aimed to eliminate the lattice curvature and produce larger pieces of flat nanogrid with square aspect ratio. This strategy, referred to as the corrugated design, causes adjacent tiles to associate with one another such that the same face of each tile is oriented up and down alternately in neighboring tiles; therefore, the surface curvature inherent in each tile should be canceled out within the assembly (see schematic drawings in Fig. 1C). Figure 1C also includes two AFM images showing the self-assembled lattice with the corrugated design. The designed distance between adjacent tile centers is 4.5 helical turns plus two DNA-helix diameters, totaling ~19.3 nm. The AFM measured distance from center to center of adja-

[1]Department of Computer Science, [2]Department of Physics, Duke University, Durham, NC 27708, USA.

*To whom correspondence should be addressed. E-mail: thl@cs.duke.edu (T.H.L); hy1@cs.duke.edu (H.Y.)